AGU100 ADVANCING EARTH AND SPACE SCIENCE

Geochemistry, Geophysics, Geosystems

RESEARCH ARTICLE
10.1029/2018GC007962

Key Points:
- We use receiver functions, ambient noise, earthquake-based surface wave, and teleseismic body wave tomography to image the Alaskan subsurface
- Shallow subduction below the Denali Volcanic Gap prevents asthenospheric flow into zones of slab fluid release, suppressing volcanism here
- The edge of the subducted Yakutat terrane delineates the easternmost extent of subduction; the Wrangell Volcanic Field lies above this edge

Supporting Information:
- Supporting Information S1

Correspondence to:
R. Martin-Short,
rmartin-short@berkeley.edu

Citation:
Martin-Short, R., Allen, R., Bastow, I. D., Porritt, R. W., & Miller, M. S. (2018). Seismic imaging of the Alaska subduction zone: Implications for slab geometry and volcanism. *Geochemistry, Geophysics, Geosystems*, *19*, 4541–4560. https://doi.org/10.1029/2018GC007962

Received 14 SEP 2018
Accepted 11 OCT 2018
Accepted article online 27 OCT 2018
Published online 21 NOV 2018

Seismic Imaging of the Alaska Subduction Zone: Implications for Slab Geometry and Volcanism

Robert Martin-Short[1], Richard Allen[1], Ian D. Bastow[2], Robert W. Porritt[3], and Meghan S. Miller[4]

[1]Berkeley Seismological Laboratory, University of California, Berkeley, CA, USA, [2]Department of Earth Science and Engineering, Imperial College London, London, UK, [3]Institute for Geophysics, Jackson School of Geosciences, University of Texas at Austin, Austin, TX, USA, [4]Research School of Earth Sciences, Australian National University, Canberra, ACT, Australia

Abstract Alaska has been a site of subduction and terrane accretion since the mid-Jurassic. The area features abundant seismicity, active volcanism, rapid uplift, and broad intraplate deformation, all associated with subduction of the Pacific plate beneath North America. The juxtaposition of a slab edge with subducted, overthickened crust of the Yakutat terrane beneath central Alaska is associated with many enigmatic volcanic features. The causes of the Denali Volcanic Gap, a 400-km-long zone of volcanic quiescence west of the slab edge, are debated. Furthermore, the Wrangell Volcanic Field, southeast of the volcanic gap, also has an unexplained relationship with subduction. To address these issues, we present a joint ambient noise, earthquake-based surface wave, and *P-S* receiver function tomography model of Alaska, along with a teleseismic *S* wave velocity model. We compare the crust and mantle structure between the volcanic and nonvolcanic regions, across the eastern edge of the slab and between models. Low crustal velocities correspond to sedimentary basins, and several terrane boundaries are marked by changes in Moho depth. The continental lithosphere directly beneath the Denali Volcanic Gap is thicker than in the adjacent volcanic region. We suggest that shallow subduction here has cooled the mantle wedge, allowing the formation of thick lithosphere by the prevention of hot asthenosphere from reaching depths where it can interact with fluids released from the slab and promote volcanism. There is no evidence for subducted material east of the edge of the Yakutat terrane, implying the Wrangell Volcanic Field formed directly above a slab edge.

Plain Language Summary We present new images of the Alaskan subduction zone that reveal the three-dimensional structure of the upper mantle and crust. Our study leverages data from a new array of high-quality seismometers, the Transportable Array, which has been deployed across the entire state. We combine multiple geophysical techniques with complementary strengths to examine the upper 150 km over a wider geographic area than has previously been imaged. This enables us to observe major changes in crustal thickness across Alaska, map the eastern edge of the subducted Yakutat-Pacific plate, and note that the enigmatic Wrangell Volcanoes lie directly above this edge, which may help to explain their unusual features. We also observe significant differences in the mantle structure beneath a volcanic region, the Aleutian Arc, and an adjacent zone of volcanic quiescence. We infer that shallow-angle subduction beneath this region has cooled the mantle here and thus limits the production of magma for volcanoes.

1. Introduction

Alaska exhibits a broad range of tectonic processes, the study of which can be used to address broader questions surrounding subduction, arc accretion, continental crust growth, and magmatism. Much of the Alaskan crust comprises rocks associated with the northern Cordilleran Orogen, which represents westward growth of the North American continent by accretion of terranes to the margin of Laurentia since the Late Triassic (Nelson & Colpron, 2007; Plafker & Berg, 1994). This process continues today with the convergence and partial subduction of the Yakutat terrane with the southern margin of Alaska, at the northeastern corner of the Pacific plate (e.g., Eberhart-Phillips et al., 2006; O'Driscoll & Miller, 2015; Plafker & Berg, 1994). This unique geometry chronicles a transition from subduction of the Pacific plate beneath North America in the west into right-lateral strike-slip motion in the east. Furthermore, the region exhibits a myriad of interesting tectonic and geodynamic processes within a relatively small area: abundant seismicity, shallow subduction, broad intraplate deformation and uplift, mantle flow around a slab edge, unusual magmatic activity in the

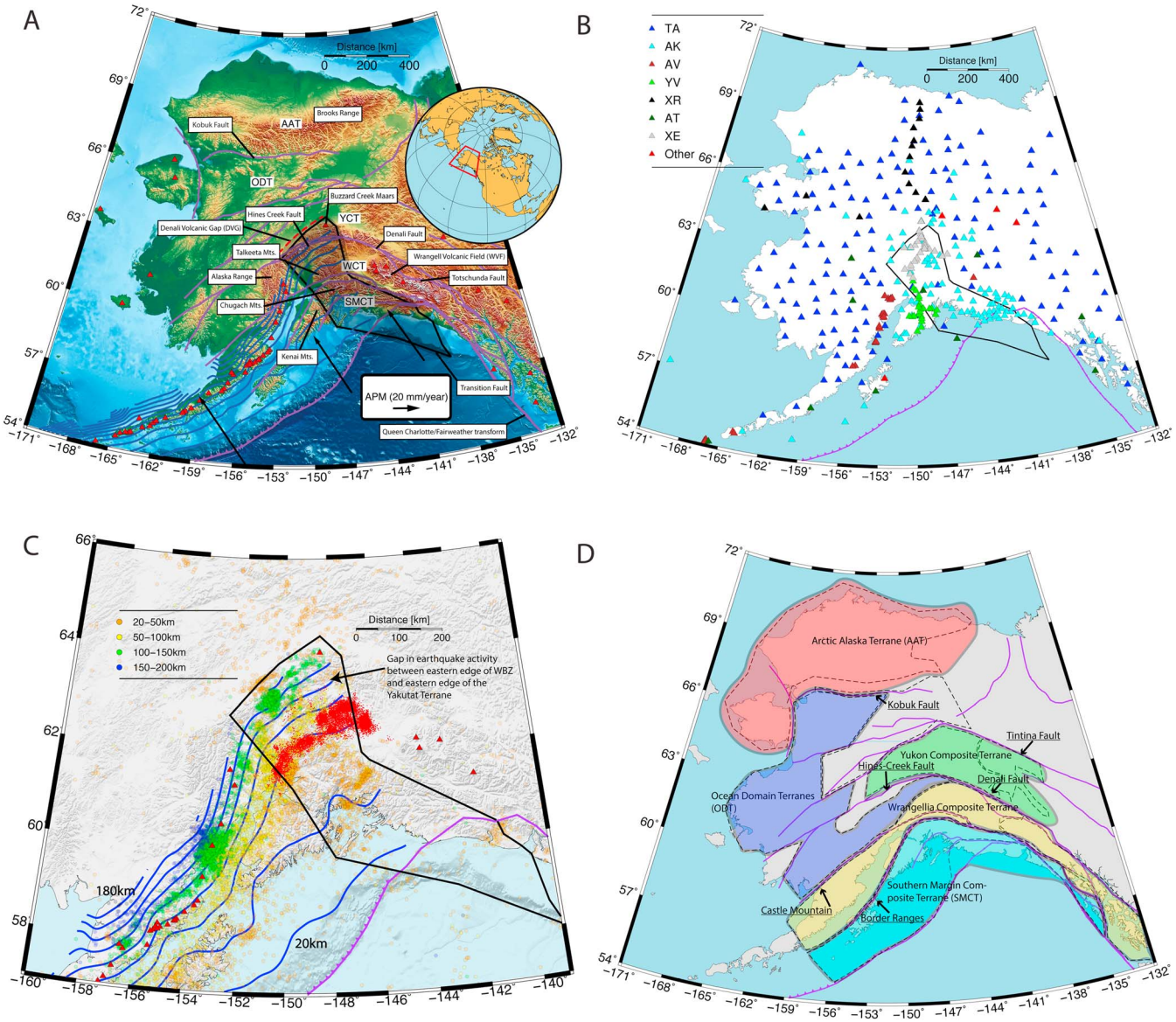

Figure 1. (a) Regional tectonic setting. Purple lines: Major active and inactive strike-slip faults (Colpron et al., 2007; see Koehler et al., 2012 for locations of active faults). Black line: The subducted extent of the Yakutat terrane as imaged by Eberhart-Phillips et al. (2006). SMCT = Southern Margin Composite Terrane; WCT = Wrangellia Composite Terrane; YCT = Yukon Composite Terrane; ODT = Ocean Domain Terrane; AAT = Arctic Alaska Terrane (Colpron et al., 2007). Purple lines contour the uppermost surface of the subducting slab at 20-km intervals, as inferred from seismicity (Hayes et al., 2012). Red triangles indicate active volcanoes. Absolute plate motion vectors were obtained from Gripp and Gordon (2002). (b) The locations of the 403 broadband seismograph station locations used in this study (coverage of Alaska as of September 2017). TA = Transportable Array (167); AK = Alaska Regional Network (113); AV = Alaska Volcano Observatory (36); YV = Multidisciplinary Observation of Subduction (23); XR = Structure and Rotation of the Inner Core (15); AT = National Tsunami Warning System (10); XE = Broadband Experiment Across the Alaska Range (31). (c) Epicenters of all $M > 3$ earthquakes in south central Alaska below 20-km depth, from the AEIC catalog. Red dots are tectonic tremor identified by Wech (2016). Blue lines are slab depth contours at an interval of 20 km (Hayes et al., 2012). (d) Map showing the boundaries of the composite terranes mentioned in this paper. Back dashed lines are terrane outlines from Colpron et al. (2007). See Text S3 for a further explanation of this map.

Wrangell Volcanic Field (WVF), and a zone of volcanic quiescence known as the Denali Volcanic Gap (DVG; Eberhart-Phillips et al., 2006; Jadamec & Billen, 2010; Martin-Short et al., 2016; Plafker & Berg, 1994; Preece & Hart, 2004; Rondenay et al., 2010; Wang & Tape, 2014).

Of these, the magmatic features are perhaps the most poorly understood: the DVG has been a region of volcanic paucity since the Miocene (Plafker & Berg, 1994). It extends ~400 km NE along strike of the subducting slab, from the eastern end of Aleutian Island Arc volcanism at Mount Spurr to the eastern terminus of the subduction zone (Figure 1a). It aligns with the northwestern edge of the subducted Yakutat terrane as

determined by Eberhart-Phillips et al. (2006). The Yakutat terrane is a portion of buoyant, overthickened (>20 km) oceanic crust, thought to have formed as an oceanic plateau (Christeson et al., 2010). Yakutat subduction is believed to have caused shallowing of the slab beneath south central Alaska (Plafker & Berg, 1994). Globally, subduction zones of overthickened crust are known to be associated with slab-flattening and volcanic gaps (e.g., Gutscher et al., 2000).

The DVG features a well-defined Wadati-Benioff Zone to ~120-km depth, likely associated with seismicity generated by the expulsion of water from hydrous minerals (Rondenay et al., 2008). The subduction style beneath the DVG differs from archetypal regions of flat-slab subduction (e.g., Nankai, Peru, and Chile) because its Wadati-Benioff Zone does not become horizontal (Chuang et al., 2017; Gutscher et al., 2000). Furthermore, several studies have argued that the sub-DVG mantle wedge may feature conditions suitable for melt production but suggest that this melt is unable to reach the surface (e.g., McNamara & Pasayanos, 2002; Rondenay et al., 2010).

The WVF lies just east of the eastern edge of the subducted Yakutat terrane (Figure 1a); it is dominated by large, andesitic shield volcanoes and calc-alkaline affinity lavas that are typical of continental volcanic arcs (Richter et al., 1990). However, the WVF also features some unusual characteristics: the presence of adakitic and tholeiitic lavas at some locations (e.g., Preece & Hart, 2004), a northwestward progression in activity over time (Richter et al., 1990) and limited seismic or tomographic evidence for an underlying slab (Martin-Short et al., 2016). These findings raise questions about the source of magma for the WFV and how it is connected to the history of Yakutat subduction, which is thought to be associated with the onset of volcanism here (e.g., Finzel et al., 2011).

Any explanation of the causes of volcanism in the WVF requires consideration of the eastern edge of the subducted Pacific-Yakutat plate, the location of which is also a subject of debate (e.g., Wech, 2016). Although the Wadati-Benioff zone terminates abruptly at ~148°W, there are multiple lines of evidence that suggest that the slab extends further east. This includes the location of the eastern edge of the Yakutat terrane as inferred from local tomography (Eberhart-Phillips et al., 2006) and the eastern limit of slab-related high-velocity anomalies seen in teleseismic surface wave (Wang & Tape, 2014) and teleseismic body wave (Martin-Short et al., 2016) tomography. Furthermore, Wech (2016) identified a zone of tectonic tremor extending 85 km east of the eastern edge of the Wadati-Benioff zone, suggesting the presence of an aseismically deforming slab (Figure 1c). It has been suggested that the slab extends further east of the tremor zone, below the WVF, but deforms by continuous slip there (Wech, 2016). This interpretation has important implications for the potential causes of volcanism here, and, given the lack of seismicity, high-resolution imaging of the upper mantle is required to locate the eastern edge of the subducting material.

The Alaskan subduction zone has been the subject of numerous seismic imaging studies. However, most utilize linear or small-aperture seismometer networks, whose resulting models do not fully map the geometry of the subducting material beneath Alaska. Recent deployment of the EarthScope Transportable Array (TA) offers an unprecedented opportunity to expand these models.

This study uses data from 405 broadband seismograph stations, including TA deployments up to September 2017 (Figure 1b). We construct an absolute *S* wave velocity model using a joint inversion of Rayleigh wave phase velocity maps from ambient noise and earthquake-based surface wave tomography in combination with *P*-*S* receiver functions calculated at each station. This joint model complements an updated version of the finite frequency, earthquake-based *S* wave relative arrival time model of Martin-Short et al. (2016), which uses data from the TA and AK networks from January 2014 to September 2017. All models presented are isotropic. Our ambient noise workflow constructs phase velocity maps for periods of 10–35 s, which are sensitive primarily to crustal velocity structure. Our earthquake-based surface wave tomography workflow generates phase velocity maps for periods 25–130 s, which are sensitive primarily to velocity structure at lower-crustal to middle-upper-mantle depths. To improve the resolution of velocity discontinuities, we use *P*-to-*S* receiver functions (Miller et al., 2018) calculated using the FuncLab software package (Eager & Fouch, 2012; Porritt & Miller, 2018).

Numerous recent studies have used joint inversion of phase velocities from ambient noise and teleseismic surface waves in regional tomography (the central Andean plateau, Ward et al., 2016; Madagascar, Pratt et al., 2017; and the Malawi rift, Accardo et al., 2017). Receiver functions have also been incorporated into

such inversions (e.g., Porritt et al., 2015). However, few studies have marshaled a combination of ambient noise, surface wave tomography, receiver functions, and body wave tomography to investigate a single region as we do here.

This paper presents the most comprehensive velocity models of the Alaskan crust and mantle to date, using them to reconcile the interpretations of previous, more geographically restricted, studies of the area. Our joint imaging approach is powerful because it harnesses the complementary strengths of each technique. However, one caveat is that it becomes difficult to accurately assess the resolution of the models because they are constructed from the inversion of multiple data sets, the uncertainties associated with which combine in a nontrivial fashion. Throughout this paper we acknowledge that confidence in our interpretation may be limited by this constraint.

Our images reveal large variations in crustal thickness across Alaska (Figures S4 and S7 in the supporting information). Furthermore, they reveal significant differences between the velocity structure of the mantle wedge beneath the volcanic region and the DVG and provide important new constraints on the eastern edge of the subducted slab.

2. Tectonic Setting

Alaska comprises a collection of terranes (Figure 1d), most of which have accreted to the western margin of North America via a combination of subduction and translation along major strike-slip faults over the past 200 Ma (Plafker & Berg, 1994; Text S1). Throughout much of the Proterozoic, Alaska lay at a passive margin at the edge of Laurentia (Colpron et al., 2007). Continental growth began with the onset of subduction in the Devonian, which brought the Yukon Composite Terrane (YCT), whose basement material had previously rifted from the margin of Laurentia, back into contact with cratonic North America by the early Triassic. Since the Cretaceous, this terrane has undergone extension and migration via right-lateral motion on the Tintina fault, which bounds it to the north (Figure 1d; Pavlis et al., 1993).

The Arctic Alaska Terrane and Ocean Domain Terrane (ODT) are located to the northwest of the YCT (Figures 1a and 1d). The former contains continental-affinity rocks of the Alaska-Arctic microplate that collided with the northern margin of Laurentia in late Jurassic time, forming the Brooks Range (Cole et al., 1997). The latter are a complex assembly of ocean-affinity terranes accreted during the Mesozoic (Nockleberg et al., 2000).

South of the Denali Fault, the Wrangellia Composite Terrane (WCT) comprises three major allochthonous terranes: Wrangellia, Alexander and Peninsular, which consist of various island arc assemblages, flood basalts, and volcanoclastic rocks (Trop & Ridgway, 2007). By the early Cretaceous, the WCT had accreted to the YCT via northward verging subduction. Subduction and consumption of the Kula plate, followed by subduction of the Pacific plate, then brought the Southern Margin Composite Terrane (SMCT; Figure 1d) into contact with North America (Colpron et al., 2007; Trop & Ridgway, 2007). This composite terrane contains mélange, scraped-off sediments, and near-trench intrusive material that form an accretionary prism. The SMCT also includes the allochthonous Yakutat terrane. Thought to have been formed as an oceanic plateau off the west coast of North America ~50 Ma, the Yakutat terrane was subsequently rafted north by dextral motion on the Queen Charlotte/Fairweather transform. It came into contact with and began subducting beneath the southern margin of Alaska as early as 35 Ma (Christeson et al., 2010; Finzel et al., 2011).

Offshore seismic reflection surveys reveal that the Yakutat crust is uniform and wedge shaped, thickening from 15 to 30 km in a west-east profile and overlain by ~8 km of sedimentary cover (Worthington et al., 2012). The Yakutat terrane is bounded to the south by the Transition fault (Figure 1a), across which there is a sharp Moho offset between ~20 Ma-old, 6 km-thick Pacific crust to ~50 Ma-old, 30 km-thick Yakutat crust (Christeson et al., 2010). The outline of the subducted Yakuat terrane, as inferred from the local tomography of Eberhart-Phillips et al. (2006), is highlighted in Figure 1a.

It is generally accepted that subduction of the thick, buoyant, downgoing Yakutat crust has reduced the dip of the downgoing plate, which in turn has led to rapid uplift of the Chugach and Alaska ranges, large-scale crustal shortening and a cessation of magmatism in the DVG. Geological and thermochronological data suggest significant uplift in south central Alaska began in late Eocene time and advanced northeastward (Finzel et al., 2011). Furthermore, magmatism above the Yakutat subduction region ceased ~32 Ma. This implies that

south central Alaska experienced steep subduction and volcanism similar to that operating in the modern Aleutian island arc before the onset of interaction with the Yakutat terrane at ~35 Ma (Finzel et al., 2011). Additionally, there is evidence that volcanism in the WVF is connected to the history of Yakutat subduction. Geochronological evidence suggests a northwestward progression of volcanic activity in the WFV, starting ~26 Ma and ceasing ~0.2 Ma (Richter et al., 1990). This led Finzel et al. (2011) to suggest that the northwestward insertion of Yakutat lithosphere beneath Alaska is responsible for WVF volcanism at the slab edge.

WVF volcanism is atypical for a subduction zone. Preece and Hart (1994) identify three geochemical trends in WVF lavas that may illuminate their origins. The first is a dominant, arc-wide suite of calc-alkaline lavas derived from a mantle wedge MORB source that experienced relatively high degree partial melting due to interaction with slab-derived fluids. A second suite of calc-alkaline lavas is restricted to *front side* volcanoes along the southeastern edge of the field. This also has a mantle wedge source, but contains adakites suggestive of slab melting (Preece & Hart, 2004). Third, a collection of tholeiitic lavas erupted from a chain of cinder cones along the central axis of the WVF are inferred to derive from low degree partial melting of anhydrous mantle wedge material in a localized extensional setting (Preece & Hart, 2004).

In contrast to the WVF, the geochemistry and physiography of the Aleutian arc are more typical of a subduction setting: calc-alkaline lava-erupting stratovolcanoes overlie the 100-km depth contour of a well-defined, steeply dipping Wadati-Benioff zone (e.g., Plafker & Berg, 1994). The position of the present-day Aleutian arc was established by ~55 Ma (Plafker & Berg, 1994), and, given the modern Pacific plate convergence rate of ~50 mm/year, several thousand kilometers of lithosphere has been subducted beneath the Aleutian arc since its formation.

3. Previous Imaging Studies

Martin-Short et al. (2016) used teleseismic *P* and *S* wave body wave tomography to image the Pacific-Yakutat slab beneath Alaska as a continuous feature. At >150-km depth, slab structure beneath the DVG is similar to that beneath the Aleutian Island arc. A high-velocity anomaly in the mantle wedge beneath the DVG, absent beneath the Aleutian arc, is only tentatively interpreted due to poor resolution in the upper 100 km of the model. Limited resolution also hampers the ability of Martin-Short et al. (2016) to interpret shallow mantle structure beneath the Wrangell Volcanoes: despite recognizing the absence of deep subduction beneath the WVF, their model cannot preclude the presence of a flat-lying or truncated slab in the upper 100 km. The surface wave tomography study of Wang and Tape (2014) reaches similar conclusions: a weak high-velocity anomaly underlies the WVF, but its relationship to the subducting Yakutat lithosphere is unresolved due to sparse instrument coverage northeast of the volcanoes. Additionally, Wang and Tape (2014) note the presence of an aseismic portion of the slab close to its eastern edge, an observation corroborated by Martin-Short et al. (2016).

Local earthquake tomography reveals the shallow structure of the Yakutat subduction zone (Eberhart-Phillips et al., 2006). The downgoing Yakutat crust is imaged as a low-velocity, high *Vp*/*Vs* layer above relatively flat-lying high-velocity lithosphere. This double layer structure is seen only beneath the DVG, where it extends to ~150-km depth, coincident with the termination of seismicity. The receiver function study of Ferris et al. (2003) and images from 2-D multichannel inversion of scattered teleseismic body waves (Rondenay et al., 2008) confirm the presence of a low-velocity zone atop the downgoing Yakutat lithosphere. This is readily interpreted as the basaltic Yakutat crust, which undergoes dehydration and transformation to eclogite, resulting in a thinning of the low-velocity zone down to 150 km, where it vanishes (Rondenay et al., 2008). Wadati-Benioff zone seismicity beneath the DVG follows a single plane, confined to the low velocity Yakutat crust. In contrast, intermediate depth seismicity within the downgoing Pacific slab to the west exhibits a thicker Wadati-Benioff zone with two planes of seismicity (Cole et al., 1997). This observation has been interpreted as differences in the hydration state of the Yakutat crust beneath the DVG and the Pacific crust beneath the volcanic arc, which may be an important step toward explaining the link between Yakutat subduction and volcanic quiescence (Chuang et al., 2017).

Stachnik et al. (2004) produce a 2-D model of the seismic attenuation structure beneath the DVG, which exhibits three distinctive regions. First, a low attenuation zone in the nose of the mantle wedge trenchward of the Denali Fault, is interpreted as cool, serpentinized material, isolated from mantle wedge convection. Second, a higher attenuation zone in the uppermost layer of the subducting lithosphere directly below the mantle

wedge nose is interpreted as fluids escaping the Yakutat crust. Finally, a high attenuation zone in the mantle wedge northwest of the Denali Fault is interpreted as hot, convecting mantle material. However, the maximum attenuation values in this region are roughly half those of the central Andes and northern Japan subduction zones, suggesting a wedge that is 100–150 °C cooler than *normal* (Stachnik et al., 2004). This observation has been suggested as an explanation for the DVG and is consistent with the high-velocity anomaly in the DVG mantle wedge imaged by Martin-Short et al. (2016). Eberhart-Phillips et al. (2006) also see a high-velocity anomaly here but interpret it as a residual slab segment from partial subduction of the WCT beneath the YCT. Such a feature could inhibit the passage of fluids and magma toward the surface, but its continuity beneath the DVG is poorly constrained.

Other studies assert that melt is present within the DVG mantle wedge but cannot reach the surface: local tomography-derived Poisson's ratios are similarly high beneath the DVG and arc volcanoes to the west (McNamara & Pasayanos, 2002), suggesting suitable melting conditions in the DVG wedge, but with melt migration arrested by increased compression in the overlying crust as a result of Yakutat collision (McNamara & Pasayanos, 2002). Rondenay et al. (2010) propose a model in which shallowing of the slab dip due to Yakutat subduction has cooled the DVG mantle wedge and prevented the accumulation of melt produced in a *pinch zone* from which it can erupt. This explains the presence of a flat-lying low-velocity zone at 60-km depth in the images of Rondenay et al. (2008), interpreted as pooling melt beneath the LAB. Rondenay et al. (2010) support their interpretation via geodynamic modeling of the evolution of the mantle wedge temperate field in the case of steady state subduction and slab advance. Given an approximation to the shallow slab geometry beneath the DVG and in the presence of temperature-dependent viscosity, slab advance acts to cool the mantle wedge and limits the focused accumulation of melt, extinguishing volcanism (Rondenay et al., 2010); slab advance associated with Yakutat subduction has thus led to a cessation of DVG volcanics.

A similar argument pertains to the eastern edge of the subducted slab beneath south central Alaska. Geodynamic modeling of mantle flow and comparison to constraints from seismic anisotropy supports the existence of deep subduction west of ~148°E, but only a short (reaching $<$115 km depth) slab beneath the WVF (Jadamec & Billen, 2010). Whether the edge of the subducted Yakutat terrane corresponds to the slab edge, or non-Yakutat lithosphere exists further to the east or beneath the WVF is unclear, with important implications for potential magma sources here.

However, the Wadati-Benioff zone terminates west of the edge of the tomographically imaged Yakutat terrane (Eberhart-Phillips et al., 2006; Martin-Short et al., 2016; Wang & Tape, 2014) and the extent of the slab as inferred by tectonic tremor (Wech, 2016). Indeed, a transition in tremor frequency from low in the west to high in the east led Wech (2016) to assert that deformation continues by continuous aseismic slip further east, connecting the seismic Pacific-Yakutat slab to an aseismic Wrangell slab. The causes of intermediate depth seismicity, or lack thereof (e.g., in Cascadia), are debated but are thought to be related to the structure and hydration state of the downgoing plate (e.g., Hacker et al., 2003). The presence of a slab edge and close proximity of hot asthenospheric material may influence the transition from seismic to aseismic deformation here, but the geometry of this boundary must be mapped to address such issues.

The receiver function studies of O'Driscoll and Miller (2015) and Bauer et al. (2014) have attempted to constrain the subduction geometry beneath Alaska by imaging velocity discontinuity structures. The *S-P* receiver function model of O'Driscoll and Miller (2015) does not resolve moderate-to-steeply dipping structures but reveals a flat Yakutat LAB at ~100-km depth beneath south central Alaska and hints at the existence of a shallow slab beneath the WVF. The plane wave migration technique employed by Bauer et al. (2014) imaged dipping features and Yakutat crust ~80 km below the WVF; the extent of the slab north of the volcanoes was unconstrained, however.

Ward (2015) used ambient noise tomography to study south central Alaska. At short periods (8–12 s), low phase velocities are associated with thick sedimentary basins such as the Cook Inlet, Kodiak Shelf and Tanana basins (Figure 4a). An elongate region of low phase velocities underlies the WVF at intermediate periods (14–25 s). The shape of this region mirrors that of a relatively low Bouguer gravity anomaly, implying compositional heterogeneity between the WVF and the surrounding crust (Ward, 2015). At 20- to 25-s period, across the Denali Fault, low velocities beneath the WCT in the south contrast with higher velocities in the north, beneath the YCT. This is interpreted as a change in crustal thickness between the terranes. A Moho offset of ~10 km near the Denali Fault has been reported by receiver function studies (e.g., Brennan et al., 2011;

Miller et al., 2018; Veenstra et al., 2006) and local tomography (Allam et al., 2017), which demonstrates the offset occurs across the Hines Creek Fault in central Alaska and the Totschunda Fault to the east. The crust thickens again further north beneath the Brooks Range (Fuis et al., 2008).

4. Data Sets and Methodology

Rayleigh wave phase velocity maps are produced using independent workflows for the ambient noise and earthquake surface wave datasets. Receiver functions were then generated for all stations (Miller et al., 2018), before being inverted jointly with the phase velocity data for absolute shear wave speed below each station. Finally, a 3-D *S* velocity map is generated by interpolation between station locations.

4.1. Ambient Noise Tomography

Continuous, daylong, long-period, vertical component seismograms from broadband stations in the region 52–73°N, 171–123°W were analyzed for the period January 2014 to September 2017 (Figure 1b). Following Bensen et al. (2008) and Ward (2015), time domain normalization with an absolute mean method and a 128-s window was applied to these data after filtering in a 5- to 150-s passband. Spectral whitening was then applied to reduce spectral imbalance and the real and imaginary components of each daylong time series were output. Station spectra were grouped into monthlong segments and cross-correlograms determined for each station-station pair. These were subsequently stacked over the maximum available timeframe. The resulting two-sided, stacked cross-correlograms are dominated by Rayleigh wave energy traveling between the stations in two directions. They can then be averaged to create a symmetric signal, which is an estimation of the Empirical Greens Function of the station-station path (Bensen et al., 2007). The dispersion characteristics of Empirical Greens Functions were determined using the FTAN method with a phase-matched filter (Levshin et al., 1992), yielding group and phase velocity dispersion curves for each station-station path at periods of 8–40 s. Dispersion curves corresponding to station pairs where one station is far outside the region of interest (Figure 2) were removed, as were dispersion measurements with a signal-to-noise ratio < 15 and an interstation distance <3 wavelengths. These criteria follow Ward (2015), but we found that varying them had little impact on the final model. The remaining dispersion measurements were then inverted for 2-D maps of phase velocity for periods of 10–35 s using the ray theoretical surface wave inversion method of Barmin et al. (2001). Resolution testing indicates that our ray coverage yields phase velocity maps able to resolve features of length scale $\geq$100 km (Figures S1–S3).

Our inversions are regularized via three user-defined parameters: The damping (α), the smoothing in regions of poor path coverage (β), and the Gaussian smoothing width (σ). Systematic variation of these parameters and inversion on a 0.1 × 0.1° grid reveals that their values do not significantly affect the results within the region of interest. Thus, we follow Ward (2015) and use $\alpha = 600$ and $\beta = 100$; σ is roughly equal to one wavelength of the inversion period. Our results are similar to those of Ward (2015) where they overlap spatially but span a larger area due to our expanded station coverage (Figure 2). Resolution tests of the ambient noise tomography are shown in Figures S1–S3.

4.2. Earthquake-Based Surface Wave Tomography

To investigate deeper velocity structure, we follow Jin and Gaherty (2015) and use the Automated Surface Wave Measuring System (ASWMS) software package to produce 25- to 130-s period fundamental mode Rayleigh wave phase velocity maps from the seismograms of teleseismic earthquakes. We analyze waveforms recorded at all stations for earthquakes of $mb > 6$ from January 2014 to September 2017 within a distance range of 20–160° (Figure S4). For each station-event pair, the Rayleigh wave and most of its coda are windowed and a cross correlation between this packet and waveforms recorded for the same earthquake at all stations within 500 km is performed. The peak of each cross-correlogram is further windowed and the periods of interest are isolated by application of narrow band-pass filters. Each filtered cross-correlogram can be represented by a five-parameter wavelet, two of whose parameters are the time-dependent group and phase delays between the two stations whose waveforms were cross correlated. For each frequency the results are inverted for the phase traveltime gradient, which is then used by the Eikonal and Helmholtz equations to produce phase velocity maps (Jin & Gaherty, 2015). Smoothing and quality control parameters in the ASWMS workflow are chosen to minimize the difference in appearance between phase velocity maps in the 25- to 35-s period range and those produced for the same period range by the ambient noise tomography

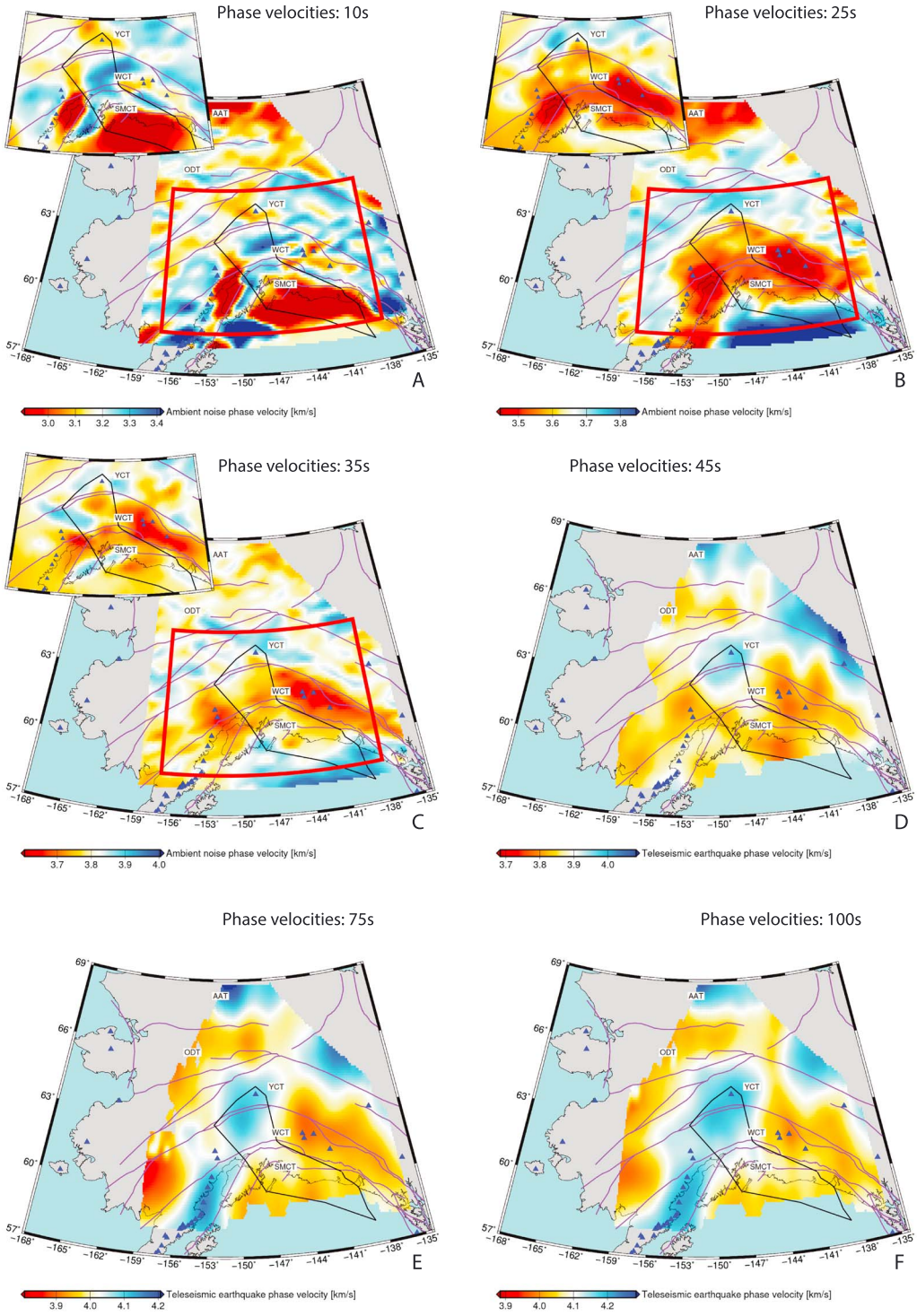

Figure 2. Rayleigh wave phase velocity maps for periods of 10 (a), 25 (b), 35 (c), 45 (d), 75 (e), and 100 s (f). Maps (a)–(c) were constructed using the ambient noise tomography workflow and corroborate the results of Ward (2015; inset maps). Maps (d)–(f) are constructed using the earthquake-based surface wave tomography workflow. Purple lines are major faults; the black line indicates the extent of the Yakutat Terrane. Blue triangles are active volcanoes. Short periods reveal variation in crustal structure, while the high-velocity subducting slab becomes increasingly apparent at longer periods. Panels (a)–(c) show the same geographic region as selected for the final velocity model, while panels (d)–(f) color only grid cells whose phase velocities are constrained by more than 10 station-event pairs. See Figure S5 for a more complete set of phase velocity maps. AAT = Arctic Alaska Terrane; YCT = Yukon Composite Terrane; WCT = Wrangellia Composite Terrane; SMCT = Southern Margin Composite Terrane; ODT = Ocean Domain Terrane.

workflow (Figures S5–S6). Phase velocity maps produced by the ASWMS workflow are sensitive to the lower crust and upper mantle at short periods; longer periods image the subducting Pacific-Yakutat plate. See Text S2 for a more complete description of the parameters used and Figure S7 for estimates of uncertainty in the phase velocity maps produced by this workflow.

4.3. Receiver Functions

Receiver functions are estimations of the Earth response function beneath a seismometer (e.g., Langston, 1979). We utilize a large database of *P-S* receiver functions determined at 468 stations in Alaska and the Yukon by Miller et al. (2018). An upgraded version of the Funclab software package (Eager & Fouch, 2012; Porritt & Miller, 2018) is used to calculate and trace edit the receiver functions. The first step involves time domain iterative deconvolution to estimate the radial Earth response, which is then multiplied by the transform of a 2.5-s-wide Gaussian pulse in the frequency domain to limit the inclusion of high-frequency signals not warranted by the observations (Langston, 1979). We supplement this data set with receiver functions for TA and AK network stations, calculated from waveforms recorded between January 2014 and September 2017. A Gaussian pulse of 1-s width damps high-frequency signals in the receiver functions, leaving them with only the direct arrival and signals from the most significant discontinuities.

In preparation for the joint inversion workflow, we follow Porritt et al. (2015) by binning the receiver functions at each station in ray parameter increments of 0.01 and back azimuth increments of 45° and stack the results in each bin.

4.4. Joint Inversion

We use the Joint96 program from the Computer Programs in Seismology software suite (Herrmann, 2013) to jointly invert the stacked *P-S* receiver functions and phase velocities from the ambient noise and earthquake-based surface wave processing workflows (Julià et al., 2000). These data sets are theoretically sensitive to the density, *P* and *S* velocity structure of the subsurface, but in practice the *S* velocity structure has the dominant influence and is hence inverted for here (e.g., Julià et al., 2000).

In the period range 25–35 s, we have phase velocities from both the ambient noise and event-based tomography. These are combined using a simple linear weighting scheme that places 100% weight on the ambient noise tomography at 25 s and 0% at 35 s. Overlap between the ambient noise and event-based phase velocity maps is imperfect (Figure 2). At the model edges some stations lack sufficient event-based phase measurements to construct a full 1-D profile; mean velocities corresponding to that period are used instead. Figures S5 and S6 show examples of the phase velocity maps included in the inversion.

Given an 82-layer initial *S* velocity model (the 1-D starting velocity model of Eberhart-Phillips et al., 2006, with a constant velocity of 4.48 km/s from the surface to 60-km depth), Joint96 conducts a series of forward calculations and linearized inversions to iterate toward a final model. Our simple starting model contains no a priori assumptions about crustal thickness, meaning the final result is entirely data driven.

Joint96 calculates Rayleigh wave depth sensitivity kernels for each of the periods represented in the phase velocity data set. At each step, these are used to forward calculate dispersion curves following Rodi et al. (1975). Synthetic receiver functions are determined using the method of Randall (1989). Residuals are calculated between the synthetic calculations and the observed data; linearized inversion is used to adjust the velocity model (Julià et al., 2000). Thirty such iterations are run, and at each step variance reduction is reported as a measure of fit between the synthetics and observations for both individual receiver functions and the data set as a whole. The result is a profile of shear velocity as a function of depth (Figure 3). We permit large departures from the initial model ($\leq$1 km/s) in the upper 100 km, where our data provide good constraints, but decrease model variance to 0 at 230-km depth. We weight our phase velocity and receiver function datasets at a ratio 25:75 during the inversion, thus placing more weight on the receiver functions (Julià et al., 2000). Variation of this parameter does not significantly affect the final velocity model (Figures S8–9). See Text S3 for the complete set of inversion parameters used.

After initial calculation of the 1-D velocity profiles, receiver functions whose reported variance reduction is $<$70% are discarded. If the variance reduction of the dispersion curve at a station is $<$70%, that station is discarded, and the Joint96 inversion is rerun. This removes the effects of noisy receiver functions, and locations where the receiver function and phase velocity data sets cannot be satisfied by a single-velocity profile.

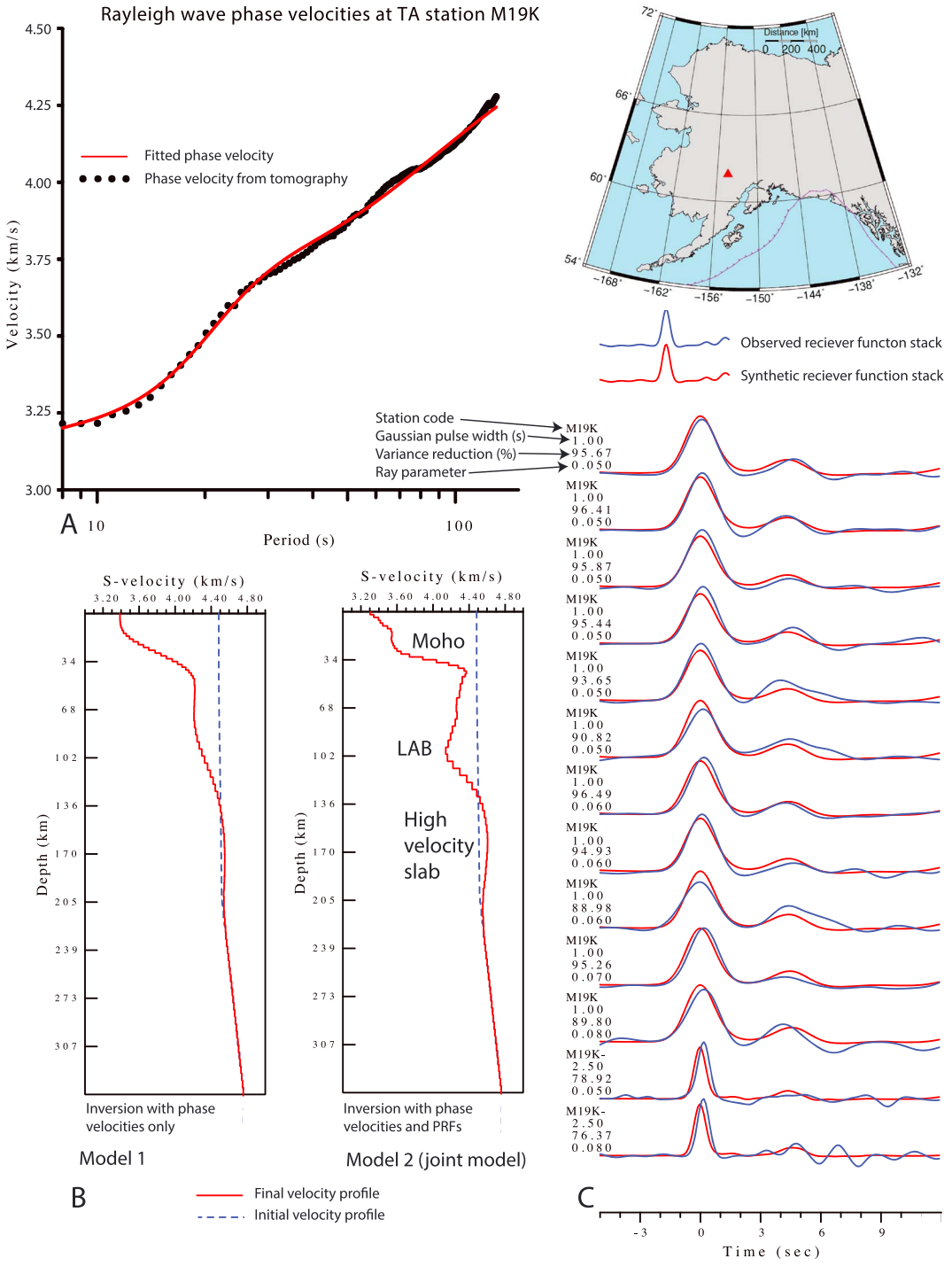

Figure 3. Example of the joint inversion workflow for station M19K, which lies above the subducting Pacific plate. (a) The fit to the phase velocity data. (b) Final velocity models constructed using just the phase velocity data (model 1) and with the addition of the receiver functions (models 2 and 3). The joint model is the preferred model because it reveals a clearer discontinuity structure. (c) The fits to the observed receiver function stacks. See Text S2 for more detailed explanation of the joint inversion procedure. TA = Transportable Array.

In some locations (e.g., offshore) receiver function data are unavailable, but velocity structure can still be constrained by the phase velocity data sets. In offshore regions, we construct a 1 × 1° grid of *ghost stations* at which the phase velocity dataset alone is used to construct 1-D velocity profiles (see Figures S1–S3 for the

offshore resolution). The same is true for a small number of onshore station locations where all the of the receiver function data is removed by the QC workflow. A map of all locations at which 1-D velocity profiles were extracted is shown in Figure S10.

The surface waves most sensitive to velocity structure >100-km depth have long periods (>100 s) and thus long wavelengths (>300 km). This causes a reduction in the lateral resolution of our joint model with depth. Consequently, we truncate our profiles at 200 km and use a relative *S* velocity model derived from finite frequency, relative arrival time body wave tomography to investigate the mantle below.

A three-dimensional (3-D) model of shear velocity to 200-km depth is constructed by linear interpolation between the 1-D profiles determined at the station locations (hereafter known as the joint model). We also construct a 3-D model using constraints from the phase velocities alone using the same station locations as in the joint inversion (hereafter known as model 2) and by linear interpolation between profiles determined on a regular grid with a spacing of 0.5° (hereafter known as model 3). There is little difference between models generated by the two interpolation strategies. However, at shallow depths, the grid-interpolation models contain more structure (Figures S11–12). Comparison of the joint model with the phase velocity-only model reveals that addition of receiver functions greatly improves our ability to identify the Moho and LAB (Figures S13 and S14).

4.5. Teleseismic Body Wave Tomography

We extend the finite frequency, relative arrival time *S* wave velocity model of Martin-Short et al. (2016) by incorporating traveltime picks for $mb > 6.0$ earthquakes recorded on AK and TA instruments between June 2016 and September 2017, at epicentral distances of 30–120°. Caution should be exercised when comparing the relative and absolute velocities (Bastow, 2012). However, the locations of these anomalies can be used to inform and support interpretations of the joint model above 200-km depth and extend our knowledge of the mantle structure below. Resolution tests of our teleseismic *S* wave model are shown in Figures S15 and S16.

5. Results

We present a series of depth slices and cross sections through the joint model and teleseismic body wave models (Figures 4–6). We color the depth slices by absolute velocity, with the color scale centered on the mean velocity at each depth. Absolute velocities in the crust and mantle are colored separately in cross sections though the joint model (Figures 5 and 6).

We identify four core observations: The pattern of velocity anomalies in the crust, variations in Moho depth across Alaska, differences in mantle wedge anomalies between the DVG and Aleutian arc, and the geometry of the subducting slab, which is inferred from the extent of a prominent high-velocity feature (Figure 4).

At shallow depths (10–20 km) we observe several regions of very low *S* wave velocity (< 3.1 km/s at 10 km), which roughly correspond to the locations of the deep Cook Inlet, Kodiak Shelf, and Colville sedimentary basins (Figure 4). Relatively high velocities are seen beneath regions of high topography, including the Alaska and Chugach ranges, the mountains of the Aleutian Arc and the eastern YCT. The central YCT contains the lowland Tanana valley region, where relatively low velocities are likely associated with the Nenana and Yukon Flats basins (Figures 4 and S12). Model 3, which comprises profiles interpolated over short distances on a regular grid, yields the most detailed images of structure at these shallow depths (Figure S12). In the case of model 2 (Figure S11) and the joint model, interpolation between velocity profiles determined at station locations tends to smooth short wavelength structure that is present in the ambient noise dataset and resolvable on the 0.5° grid.

At lower-crustal depths (30–45 km) we see several long wavelength anomalies (Figures 4, S11, and 12). There is a dramatic contrast between low velocities south of the central part of the Denali Fault and high velocities to the north. Onshore velocities are highest below the lowlands of the Tanana basin and decrease again below the high topography of the Brooks Range. The lowest velocities are seen beneath the Aleutian Island arc, Chugach Mountains, and WVF, corroborating phase velocity maps at intermediate periods (14–25 s) constrained by Ward (2015). The highest velocities are found offshore, beneath the Pacific plate.

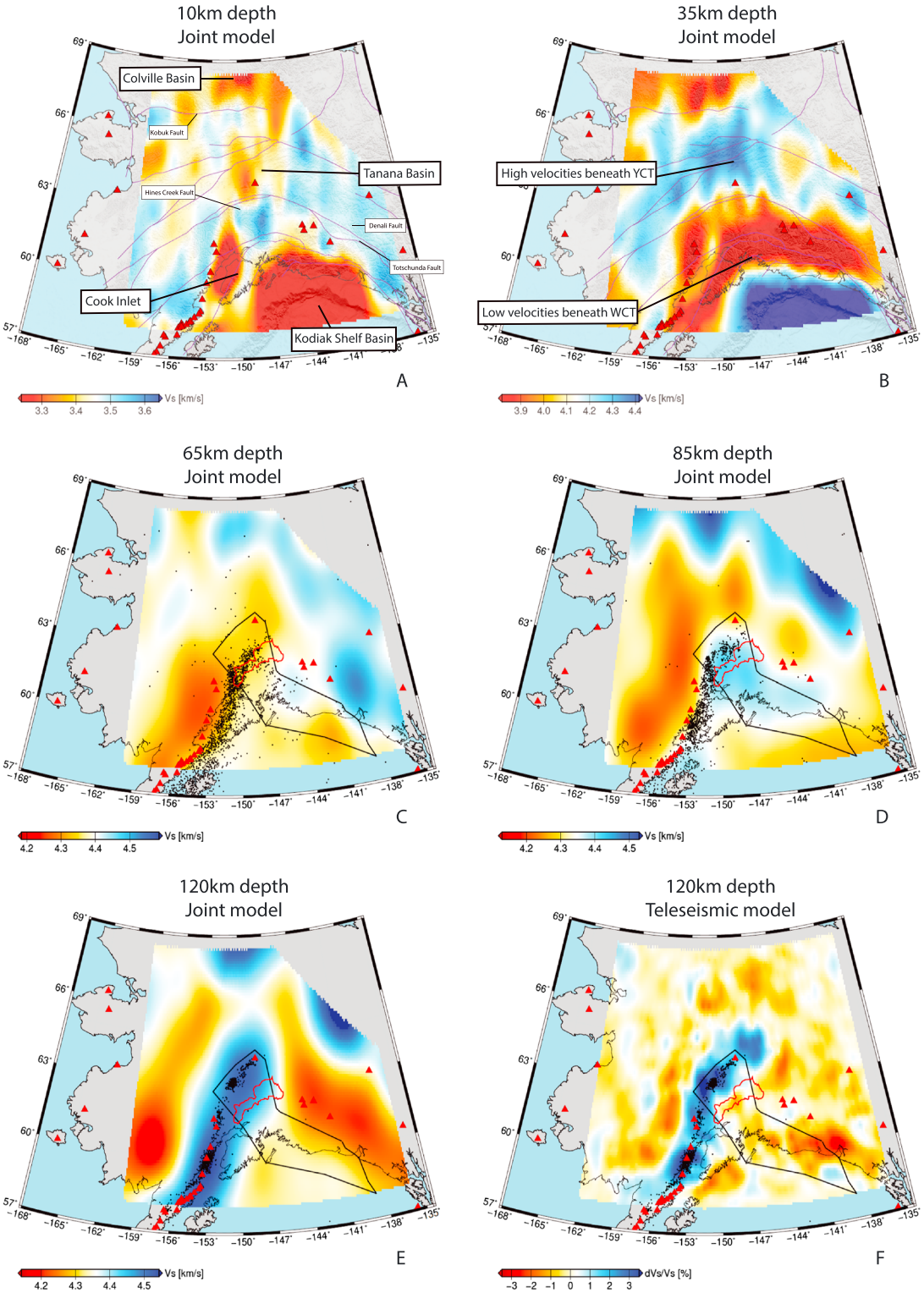

Figure 4. Slices though the joint model at depths of 10 (a), 35 (b), 65 (c), 85 (d), and 120 km (e), which reveal large-scale variations in the crust and uppermost mantle beneath Alaska. Black dots are $M > 3.0$ earthquake hypocenters within ±5 km of the depth slices. Topography contours are displayed in (a) and (b) to illustrate the connection between tomography and crustal velocity structure. Faults (purple lines) in (b) indicate differences in velocity across major terrane boundaries. The red outline in panels (c)–(f) indicates the zone of tectonic tremor identified by Wech (2016), whose eastern boundary aligns with the edge of the high-velocity slab. The black line delineates the subducted Yakutat terrane. Red triangles are active volcanoes. (f) The 120-km depth slice though the teleseismic finite frequency *S* body wave, which a shows a broadly similar structure to map (e). YCT = Yukon Composite Terrane; WCT = Wrangellia Composite Terrane.

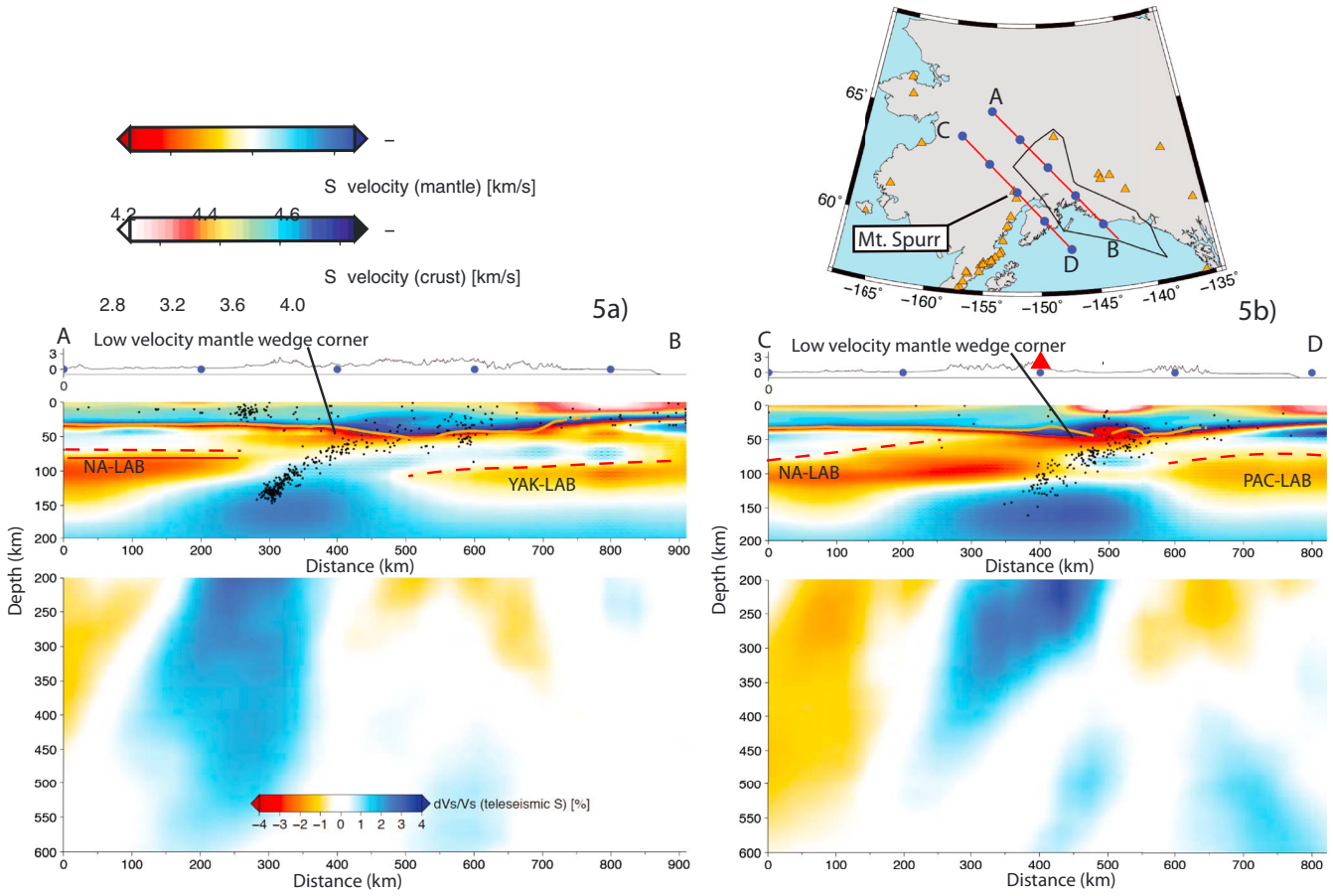

Figure 5. Cross sections from the joint model (0- to 200-km depth) and teleseismic *S* model (200- to 600-km depth) though the Denali Volcanic Gap (a) and Aleutian Arc (b). The absolute velocity structure of the crust and mantle is mapped with two different color schemes, spanning 2.65–4.1 and 4.1–4.65 km/s, respectively. The orange line is the continental Moho as inferred from the joint model (Figure S15). Black dots are earthquake hypocenters within ±20 km of the slices. Annotations on the joint model slice are our tectonic interpretations.

A low-resolution map of continental Moho depth can be generated from the joint model by identifying the depth of maximum velocity gradient at each station location where receiver functions are available and then fitting these values with a continuous surface (Figure S17). We force this method to pick a Moho between 20- and 60-km depth, thereby avoiding picking of the oceanic Moho in regions where oceanic crust is directly overlain by continental crust, as is the case throughout the SMCT. The map is necessarily smooth due to the station spacing, but reveals the presence of an arc of thick crust (>50 km) beneath the Chugach mountains, a transition between relatively thick (>35 km) to thin (~25 km) crusts across the central Denali Fault and a return to thick crust (>40 km) below the Brooks Range. Moho picks from the joint velocity model are in good agreement with those determined directly from the *P-S* receiver functions by Miller et al. (2018; Figures S18–20). Furthermore, the differences in Moho depth between receiver function only and joint receiver function-surface wave inversion methodologies can often be on the order of those observed here (e.g., in Cameroon: Gallacher & Bastow, 2012).

In the uppermost mantle we observe several notable features. A low-velocity anomaly in the mantle wedge west of the Aleutian arc at ~60-km depth persists to >100 km (Figures 4c and 4d). This feature is also present, but less pronounced, in the mantle wedge beyond the northwestern edge of the subducted Yakutat terrane. A low-velocity anomaly at 60-km depth beneath the northeastern edge of the WVF becomes broader and more pronounced with depth, where it connects with the low velocities in the mantle wedge north of the subduction zone. This creates a channel of low-velocity material that separates high-velocity features in the far north and east of the model region from those in south central Alaska.

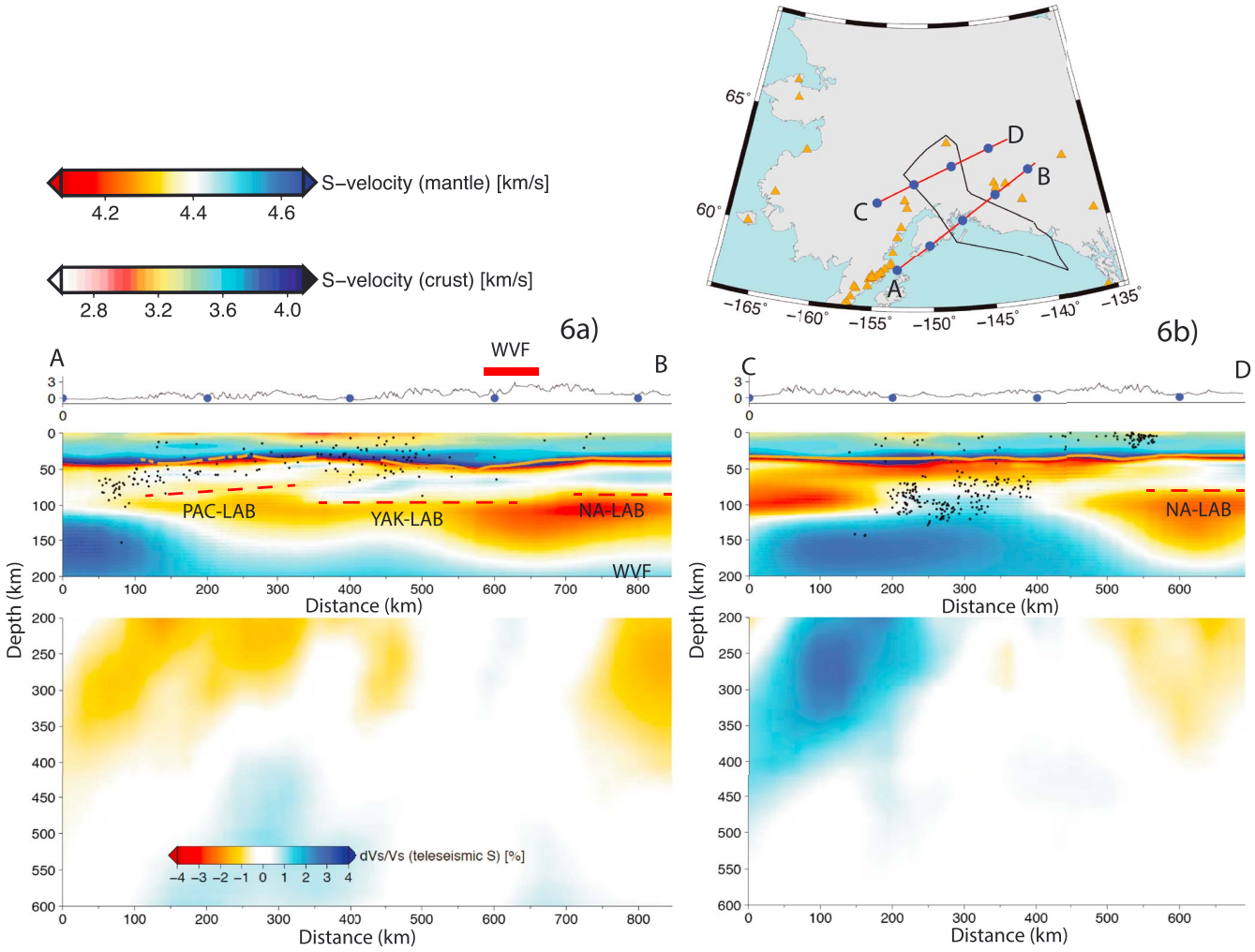

Figure 6. Cross sections from the joint and teleseismic models. (a) Taken across the northwestern extent of the Yakutat terrane; (b) taken perpendicular to the strike of the Wrangell Volcanic Field. The color scheme and symbols are the same as described in Figure 5. Our interpretation of the velocity structure is shown on the joint model cross sections.

A broad high-velocity feature is seen within the boundaries of the subducted Yakutat terrane (Figure 4d). It appears at ~70-km depth in the southeast and, with increasing depth, spreads north and west to become an elongate high-velocity feature that extends along the Aleutian arc and broadens beneath south central Alaska. The western edge of this feature parallels the Wadati-Benioff zone; its east facing edge is aligned with the tectonic tremor zone identified by Wech (2016). Furthermore, the WVF is orientated along the northeast facing edge of this zone (Figure 4).

We interpret this high-velocity anomaly as the subducting Pacific-Yakutat lithosphere (Figure 4). Below ~100-km depth, the slab anomaly within the joint model is subject to significant lateral smearing but its geometry is consistent with that of the slab as inferred from the teleseismic body wave model (Figure 4f). This consistency is especially clear in cross section (e.g., Figure 5).

6. Discussion

The large spatial extent of our velocity model and its use of complementary imaging techniques allow us to provide an interpretation of the tectonic structure beneath central Alaska throughout the crust and upper mantle.

6.1. Crustal Structure and Moho Depth Variations

At shallow depths, the lowest velocities are located within the ≥8-km-deep Cook Inlet and Kodiak shelf sedimentary basins (Christeson et al., 2010; Shellenbaum et al., 2010). Moderately low velocities characterize other major Cenozoic sedimentary basins (Figures 4a, S11, and S12). The highest velocities are seen beneath the Chugach, Kenai and Talkeetna Mountains, which comprise layers of intermediate to ultramafic material, thought to be accreted slivers of oceanic crust (Ferris et al., 2003). High velocities also characterize the Aleutian arc and western Yukon-Tanana uplands, where they likely indicate the high-grade metamorphic or igneous cores of these elevated regions.

In most locations, our model lacks the necessary resolution to map potentially abrupt steps in crustal thickness across terrane boundaries (e.g., Allam et al., 2017; Miller et al., 2018). However, our maps, cross sections and Moho depth calculations confirm that significant crustal thickness variations exist from terrane to terrane (Figures 3, S11, 12, S17, and S21). Despite not being constrained by receiver functions, the Pacific-Yakutat crust offshore is observed to be relatively thin compared to that of North America, hence explaining the presence of mantle velocities offshore in the 35-km depth slice (Figure 4b). The continental crust beneath the WCT and SMCT is relatively thick, especially beneath the Chugach Mountains and south of the WVF, where it exceeds 50 km (Figure S17). This is consistent with previous observations of Moho depth in this region (Christeson et al., 2010; Eberhart-Phillips et al., 2006; Miller et al., 2018) and is probably the result of Yakutat underplating of the WCT (Christeson et al., 2010).

The sharp velocity contrast between the WCT and YCT across the Denali Fault in central and eastern Alaska at 35-km depth (Figure 4b) is interpreted as a Moho step. This is consistent with previous studies, which consistently report that crust below the Tanana Basin is some of the thinnest in Alaska (e.g., Miller et al., 2018; Veenstra et al., 2006) and is offset from the thick crust to the south along the Hines Creek Fault (Allam et al., 2017). This offset is most dramatic close to where the Broadband Experiment Across the Alaska Range array crosses the terrane boundary, but continues west along the Hines Creek Fault and then south on the landward side of the Aleutian arc (Figure 4). There is no abrupt change in velocity between the YCT and ODT, but the sharp decrease in velocity seen across the Kobuk fault zone (Figure 4), which bounds the Arctic Alaska and ODT, indicates crustal thickening beneath the Brooks Range, consistent with the findings of Miller et al. (2018).

6.2. Mantle Wedge and DVG

Figures 5 and S19 show cross sections through the velocity structure of the DVG (Figure 5a) and the Aleutian island arc near Mount Spurr (Figure 5b). These indicate the slab and continental LAB locations, which are inferred from velocity discontinuities and agree with LAB picks from O'Driscoll and Miller (2015) where the models overlap (Figure S21).

The slab is imaged as a dipping, high-velocity (4.4–4.6 km/s) structure whose uppermost surface is delineated by a Wadati-Benioff zone. The slab geometry and velocity values are consistent with the models of Wang and Tape (2014) and Eberhart-Phillips et al. (2006). The latter study has higher resolution but is more restricted spatially. Velocities in the mantle wedge are relatively low (4.2–4.3 km/s) and overlain by a zone of higher velocities (4.3–4.5 km/s), interpreted as continental lithosphere. In both cases there is a region of very low velocities (4.1–4.2 km/s) at the nose of the mantle wedge at depths of 40–60 km (corresponding to ~1.2–1.8GPa), directly above a high seismicity zone that likely marks the onset of eclogitization (Chuang et al., 2017; Rondenay et al., 2008). The large volume change that accompanies eclogitization of the downgoing oceanic crust is thought to promote fluid release into the mantle wedge (Audet et al., 2009). At the cool (< 600 °C) mantle wedge nose, hydration of peridotite leads to the formation of the serpentine mineral antigorite, the presence of which can depress seismic velocities (e.g., Christensen, 1996). We interpret the low velocity mantle forearc in Figures 5a and 5b to indicate the presence of fluids and the formation of antigorite. Evidently, the degree of serpentinization is low in comparison to Cascadia, because the receiver functions do not indicate an inverted Moho as is there (Bostock et al., 2002). These findings support the interpretation of Stachnik et al. (2004), who attribute a high-Q region in the DVG mantle forearc to serpentinization. The *Vp*/*Vs* model of Rossi et al. (2006) also indicates ≤30% serpetinization within the nose of the DVG mantle wedge. Our models indicate that this serpentinized nose is present in both the volcanic and nonvolcanic zones.

In both cross sections, a continental LAB caps the low velocity mantle wedge asthenosphere. Below the volcanogenic region, the LAB dips northward in such a way that it disappears beneath the Aleutian arc volcanoes (Figure 5b). In contrast, the continental LAB beneath the DVG is horizontal at ~70-km depth, thus separating the low-velocity mantle wedge asthenosphere from the serpentinized forearc mantle at shallower depths (Figure 5a). The location of this horizontal LAB is similar to that of the horizontal low velocity anomaly seen below the DVG in the images of Rondenay et al. (2008), which they interpret as pooled melt below an impermeable mantle layer. This supports the suggestion of Chuang et al. (2017) that the Rondenay et al. (2008) low-velocity anomaly is an expression of the continental LAB, where dry lithosphere overlies hydrated asthenosphere. Our model resolution is insufficient to rule out the melt-pocket interpretation, however, and it remains compatible with our discussion.

In the Aleutian Arc cross section (Figure 5b), the dipping LAB allows low velocity mantle wedge material much closer to the surface than the horizontal LAB beneath the DVG. We interpret this low velocity region as convecting, hot asthenosphere. In the volcanogenic zone, it is present in the mantle directly below the volcanoes, above the 100-km depth contour of the downgoing slab. Fluids being released from eclogitizing oceanic crust thus enter this zone and contribute to melt production and volcanism. In contrast, the paucity of low-velocity mantle wedge material above the 100-km slab depth contour within the DVG suggests that the mantle wedge there is relatively isolated from asthenospheric circulation and may not be warm enough to generate sufficient melt to cause volcanism, even if slab-derived fluids are present. This is consistent with the Q tomography of Stachnik et al. (2004), which suggests that the DVG mantle wedge is anomalously cool. Cooling of the wedge and isolation from circulation can be attributed to shallowing of the slab dip angle due to subduction of the thick Yakutat crust, as indicated by the geodynamic modeling of Rondenay et al. (2010). Localized melt production must still occur in this region as evidenced by the presence of the Buzzard Creek Maars cinder cones (Figure 1a).

The DVG mantle wedge may also be deprived of slab-derived fluids relative to the Aleutian arc mantle wedge, which could further help to explain the observed pattern of anomalies.

Chuang et al. (2017) propose the Yakutat water budget is confined to the uppermost oceanic crust, rendering the Yakutat terrane relatively anhydrous compared to the adjacent Pacific plate. Thus, most fluid is released over a relatively small depth range (60–80 km), where *P-T* conditions prevent it from catalyzing melt production. If the catalyzing fluids are restricted to shallow depths, metagabbros in the mid-Yakutat crust can remain metastable to $>$100 km depth, below which they experience accelerated eclogitization at pressures far above equilibrium (Chuang et al., 2017).

Our model does not constrain the relative hydration states of Yakutat and Pacific crust nor does it allow us to distinguish between low-velocity zones resulting from fluid or melt. Nevertheless, the Chuang et al. (2017) interpretation, which elucidates previously unexplained characteristics of DVG seismicity, is compatible with our observations. Consequently, we suggest that a combination of low mantle wedge temperatures due to relative isolation from asthenosphere circulation, and low-fluid content due to shallow dehydration of the Yakutat crust, explain the lack of volcanism in the DVG and its association with the Yakutat terrane.

6.3. Eastern Slab Edge and WVF

The teleseismic tomography model indicates that the deep ($>$150 km) slab terminates abruptly and does not extend past 148°W. This likely has important implications for asthenospheric flow (e.g., Jadamec & Billen, 2010). The eastern edge of the subducted material above 150-km depth corresponds to the eastern edge of the Yakutat terrane as imaged by Eberhart-Phillips et al. (2006; Figures 4 and 6). We interpret the broad high-velocity zone that appears within the boundaries of the Yakutat terrane to be the subducted Yakutat lithosphere, which is connected to the subducted Pacific lithosphere in a continuous arc. Given approximate ages of 50 Ma for the Yakutat terrane and 20 Ma for the adjacent Pacific plate, a simple conductive cooling calculation reveals that the Yakutat lithosphere should be ~25 km thicker than Pacific lithosphere. This may explain why the Yakutat lithosphere is more prominent in our models (Figures 4 and 5).

Although the Wadati-Benioff zone terminates ~85 km west of the eastern edge of the subducted material, the end of tectonic tremor zone identified by Wech (2016) is well aligned with this edge (Figure 4d). The tremor zone occurs at depths of 50–80 km, and the interevent time increases from ~10 days in the west to ~3 hr in the east. Wech (2016) suggests that this increase in tremor frequency documents a transition from periodic

slip to continuous aseismic slip. However, we see no evidence for subducted material east of the eastern edge of the tremor zone and thus conclude this is the true slab edge. The lack of a Wadati-Benioff zone and increase in tremor frequency could thus be explained by heating of the slab edge by the adjacent hot asthenosphere.

Figures 4d and 6 suggest that the southeast to northwest trending WVF lies directly above the truncated edge of the subducted Yakutat Terrane. This is compatible with the observations of previous studies (e.g., Bauer et al., 2014; O'Driscoll & Miller, 2015), which also note the presence of subducted lithosphere beneath the WVF. However, these studies infer that the subducting material also extends northeast of the WVF, as would be the case in a typical subduction zone. We see no evidence for a Wrangell slab that extends northeast of the WVF in our models. Instead, we observe a horizontal Yakutat LAB that terminates directly below the WVF (Figure 6a). This is consistent with the *SKS* splitting observations of Witt (2016), which reveal a dramatic change in fast axis orientation across the axis of the WVF. This could be interpreted as a transition between subslab flow to flow in the asthenosphere beyond the slab edge, which parallels North American absolute plate motion. However, we acknowledge that our inability to conduct resolution tests on the joint model must limit our confidence in these interpretations.

Northeast of the edge of the Yakutat terrane, which is interpreted as the edge of the subducted material, lies a zone of low-velocity (4.1–4.3 km/s) asthenosphere. This is capped by relatively fast (4.4–4.5 km/s) material at ~70-km depth, interpreted as continental lithosphere (Figure 6). Geodynamic modeling predicts quasi-toroidal mantle flow around the sharp edge of the Pacific-Yakutat slab should lead to upwelling beneath the WVF, explaining volcanism there (Jadamec & Billen, 2010, 2012). The presence of a low-velocity zone just northwest of the volcanoes supports this idea. We assert that the unusual geochemical and physiographical characteristics of the WVF, in addition to its northwestward advance over the past 23 Ma, can be explained by processes occurring at the truncated edge of the Yakutat terrane and their interaction with hot, upwelling asthenosphere. The arc-wide suite of calc-alkaline lavas identified by Preece and Hart (2004) could be explained by interaction between fluids derived from the Yakutat crust, and this high-temperature asthenosphere. Melting of the slab edge itself would also explain the presence of adakites along the south facing edge of the WVF (Preece & Hart, 2004). The northwestward insertion of the Yakutat terrane beneath North America may have been associated with the formation of transtensional basins within the WVF (Finzel et al., 2011), which in turn provide a suitable environment for the eruption of the tholeiitic lavas reported by Preece and Hart (2004).

7. Conclusions

We have presented a new absolute velocity model of the Alaskan subduction zone by jointly inverting receiver functions and phase velocities from ambient noise tomography and earthquake-based surface wave tomography. This complements an updated version of the finite frequency, teleseismic *S* wave relative arrival time tomography model of Martin-Short et al. (2016). Recent deployment of the TA in Alaska permits the construction of tomography models of sufficient geographic extent to investigate differences between mantle wedge structure below the DVG and adjacent Aleutian arc, and to map the geometry of the eastern edge of the slab. We draw three fundamental conclusions:

1. There is a significant difference in crustal thickness between the Southern Composite Terranes (SMCT and WCT) and YCT, which lies to the north of the Denali Fault. The largest offset occurs in central Alaska, where the Tanana Basin lies adjacent to the Alaska Range. This has been noted by previous localized studies (e.g., Allam et al., 2017; Miller et al., 2018; Veenstra et al., 2006; Ward, 2015), but we are the first to observe it in a large-scale velocity model. The thickest crust in Alaska (50–55 km) is found beneath the Chugach range, where crustal thickening may be the result of underplating of material from the subducting Yakutat terrane (e.g., Christeson et al., 2010).
2. A reduction in slab dip caused by the introduction of thick, buoyant Yakutat crust to the subduction zone has cooled the mantle wedge below the DVG, thickening the continental lithosphere here and thus preventing hot, convecting asthenosphere mixing with slab-derived fluids at depths where they could promote extensive melting. This contrasts with the steeper dip of the subducting Pacific plate to the west. Our interpretation is similar to that made by Rondenay et al. (2010) and supported by their geodynamic modeling.

3. We provide new constraints on the geometry of the eastern edge of the subducting slab, although our confidence is limited by an inability to conduct resolution tests on the joint model. The edge of the Yakutat terrane, as inferred from the crustal model of Eberhart-Phillips et al. (2006), closely aligns with the edge of the high-velocity slab, and with the eastern limit of the tectonic tremor region (Wech, 2016). We see no evidence for subducted material east of the Yakutat terrane, implying the WVF lies directly above the truncated, northeastward facing edge of the Yakutat terrane. Adjacent to this edge is a low-velocity (4.2–4.3 km/s) zone, interpreted as hot, potentially upwelling, asthenosphere. Melting of the slab edge by this material, interaction with fluids derived from the Yakutat crust, and extension of the overlying crust within transtensional basins, may explain the unusual geochemistry and age progression of the WVF.

Finally, our model provides a platform on which further imaging studies of this region can build. Such work could, for example, seek to quantify the uncertainties in our joint model though a Monte-Carlo inversion approach (e.g., Shen et al., 2013). The resolution of our models might also be improved through the joint inversion of Rayleigh wave group, Love wave phase, and group velocities along with the Rayleigh phase observations made here. Future studies might also seek to jointly invert body and surface wave observations to produce a single model capable of resolving features from the crust to the mantle transition zone in order to gain a more self-consistent picture of the subduction zone at a large scale.

Acknowledgments
We thank C. Tape and one anonymous reviewer for helpful comments. All seismograms come from the Incorporated Research Institutions for Seismology (IRIS) Data Management Center, which is funded through the Seismological Facilities for the Advancement of Geoscience and EarthScope (SAGE) Proposal of the National Science Foundation under Cooperative Agreement EAR-126168. TA network data were made freely available as part of the EarthScope USArray facility, operated by IRIS and supported by the National Science Foundation, under Cooperative Agreements EAR-1261681. Ambient noise phase velocities were constructed using CU-Boulder software (http://ciei.colorado.edu/Products/). Earthquake-derived phase velocities were determined using the ASWMS software (https://ds.iris.edu/ds/products/aswms). Figures were created using the Generic Mapping Tools (Wessel & Smith, 1998).

References

Accardo, N. J., Gaherty, J. B., Shillington, D. J., Ebinger, C. J., Nyblade, A. A., Mbogoni, G. J., et al. (2017). Surface wave imaging of the weakly extended Malawi rift from ambient-noise and teleseismic Rayleigh waves from onshore and lake-bottom seismometers. *Geophysical Journal International*, *209*(3), 1892–1905. https://doi.org/10.1093/gji/ggx133

Allam, A. A., Schulte-Pelkum, V., Ben-Zion, Y., Tape, C., Ruppert, N., & Ross, Z. E. (2017). Ten kilometer vertical Moho offset and shallow velocity contrast along the Denali fault zone from double-difference tomography, receiver functions, and fault zone head waves. *Tectonophysics*, *721*, 56–69. https://doi.org/10.1016/j.tecto.2017.09.003

Audet, P., Bostock, M. G., Christensen, N. I., & Peacock, S. M. (2009). Seismic evidence for overpressured subducted oceanic crust and megathrust fault sealing. *Nature*, *457*(7225), 76–78. https://doi.org/10.1038/nature07650

Barmin, M. P., Ritzwoller, M. H., & Levshin, A. L. (2001). A fast and reliable method for surface wave tomography. *Pure and Applied Geophysics*, *158*(8), 1351–1375. https://doi.org/10.1007/PL00001225

Bastow, I. D. (2012). Relative arrival-time upper-mantle tomography and the elusive background mean. *Geophysical Journal International*, *190*(2), 1271–1278. https://doi.org/10.1111/j.1365-246X.2012.05559.x

Bauer, M. A., Pavlis, G. L., & Landes, M. (2014). Subduction geometry of the Yakutat terrane, southeastern Alaska. *Geosphere*, *10*(6), 1161–1176. https://doi.org/10.1130/GES00852.1

Bensen, G. D., Ritzwoller, M. H., Barmin, M. P., Levshin, A. L., Lin, F., Moschetti, M. P., et al. (2007). Processing seismic ambient noise data to obtain reliable broad-band surface wave dispersion measurements. *Geophysical Journal International*, *169*(3), 1239–1260. https://doi.org/10.1111/j.1365-246X.2007.03374.x

Bensen, G. D., Ritzwoller, M. H., & Shapiro, N. M. (2008). Broadband ambient noise surface wave tomography across the United States. *Journal of Geophysical Research*, *113*, B05306. https://doi.org/10.1029/2007JB005248

Bostock, M. G., Hyndman, R. D., Rondenay, S., & Peacock, S. M. (2002). An inverted continental moho and serpentinization of the forearc mantle. *Nature*, *417*(6888), 536–538. https://doi.org/10.1038/417536a

Brennan, P. R. K., Gilbert, H., & Ridgway, K. D. (2011). Crustal structure across the central Alaska Range: Anatomy of a Mesozoic collisional zone. *Geochemistry, Geophysics, Geosystems*, *12*, Q04010. https://doi.org/10.1029/2011GC003519

Christensen, N. I. (1996). Poisson's ratio and crustal seismology. *Journal of Geophysical Research*, *101*(B2), 3139–3156. https://doi.org/10.1029/95JB03446

Christeson, G. L., Gulick, S. P. S., van Avendonk, H. J. A., Worthington, L. L., Reece, R. S., & Pavlis, T. L. (2010). The Yakutat terrane: Dramatic change in crustal thickness across the transition fault, Alaska. *Geology*, *38*(10), 895–898. https://doi.org/10.1130/G31170.1

Chuang, L., Bostock, M., Wech, A., & Plourde, A. (2017). Plateau subduction, intraslab seismicity, and the Denali (Alaska) volcanic gap. *Geology*, *45*(7), 647–650. https://doi.org/10.1130/G38867.1

Cole, F., Bird, K. J., Toro, J., Roure, F., O'Sullivan, P. B., Pawlewicz, M., & Howelll, D. G. (1997). An integrated model for the tectonic development of the frontal Brooks Range and Colville Basin 250 km west of the Trans-Alaska Crustal Transect. *Journal of Geophysical Research*, *102*(B9), 20,685–20,708. https://doi.org/10.1029/96JB03670

Colpron, M., Nelson, J. A. L., & Murphy, D. C. (2007). Northern cordilleran terranes and their interactions through time. *GSA Today*, *17*(4), 4–10. https://doi.org/10.1130/GSAT01704-5A.1

Eager, K. C., & Fouch, M. J. (2012). FuncLab: A MATLAB interactive toolbox for handling receiver function datasets. *Seismological Research Letters*, *83*(3), 596–603. https://doi.org/10.1785/gssrl.83.3.596

Eberhart-Phillips, D., Christensen, D. H., Brocher, T. M., Dutta, U., Hansen, R., & Ratchkovski, N. A. (2006). Imaging the transition from Aleutian subduction to Yakutat collision in central Alaska, with local earthquakes and active source data. *Journal of Geophysical Research*, *111*, B11303. https://doi.org/10.1029/2005JB004240

Ferris, A., Abers, G. A., Christensen, D. H., & Veenstra, E. (2003). High resolution image of the subducted Pacific (?) plate beneath Central Alaska, 50-150 km depth. *Earth and Planetary Science Letters*, *214*(3–4), 575–588. https://doi.org/10.1016/S0012-821X(03)00403-5

Finzel, E. S., Trop, J. M., Ridgway, K. D., & Enkelmann, E. (2011). Upper plate proxies for flat-slab subduction processes in southern Alaska. *Earth and Planetary Science Letters*, *303*(3–4), 348–360. https://doi.org/10.1016/j.epsl.2011.01.014

Fuis, G. S., Moore, T. E., Plafker, G., Brocher, T. M., Fisher, M. A., Mooney, W. D., et al. (2008). Trans-Alaska crustal transect and continental evolution involving subduction underplating and synchronous foreland thrusting. *Geology*, *36*(3), 267–270. https://doi.org/10.1130/G24257A.1

Gallacher, R., & Bastow, I. (2012). The development of magmatism along the Cameroon Volcanic Line: Evidence from teleseismic receiver functions. *Tectonics*, *31*, TC3018. https://doi.org/10.1029/2011TC003028

Gripp, A. E., & Gordon, R. G. (2002). Young tracks of hotspots and current plate velocities. *Geophysical Journal International*, *150*(2), 321–361. https://doi.org/10.1046/j.1365-246X.2002.01627.x

Gutscher, M. A., Maury, R., Eissen, J. P., & Bourdon, E. (2000). Can slab melting be caused by flat subduction? *Geology*, *28*(6), 535–538. https://doi.org/10.1130/0091-7613(2000)28<535:CSMBCB>2.0.CO;2

Hacker, B. R., Peacock, S. M., Abers, G. A., & Holloway, S. D. (2003). Subduction factory 2. Are intermediate-depth earthquakes in subducting slabs linked to metamorphic dehydration reactions? *Journal of Geophysical Research*, *108*(B1), 2030. https://doi.org/10.1029/2001JB001129

Hayes, G. P., Wald, D. J., & Johnson, R. L. (2012). Slab1.0: A three-dimensional model of global subduction zone geometries. *Journal of Geophysical Research*, *117*, B01302. https://doi.org/10.1029/2011JB008524

Herrmann, R. B. (2013). Computer Programs in Seismology: An evolving tool for instruction and research. *Seismological Research Letters*, *84*(6), 1081–1088. https://doi.org/10.1785/0220110096

Jadamec, M., & Billen, M. I. (2012). The role of rheology and slab shape on rapid mantle flow: Three-dimensional numerical models of the Alaska slab edge. *Journal of Geophysical Research*, *117*, B02304. https://doi.org/10.1029/2011JB008563

Jadamec, M. A., & Billen, M. I. (2010). Reconciling surface plate motions with rapid three-dimensional mantle flow around a slab edge. *Nature*, *465*(7296), 338–341. https://doi.org/10.1038/nature09053

Jin, G., & Gaherty, J. B. (2015). Surface wave phase-velocity tomography based on multichannel cross-correlation. *Geophysical Journal International*, *201*(3), 1383–1398. https://doi.org/10.1093/gji/ggv079

Julià, J., Ammon, C. J., Herrmann, R. B., & Correig, A. M. (2000). Joint inversion of receiver function and surface wave dispersion observations. *Geophysical Journal International*, *143*(1), 99–112. https://doi.org/10.1046/j.1365-246x.2000.00217.x

Koehler, R. D., Rebecca-Ellen, F., Burns, P. A. C., & Combellick, R. A. (2012). Quaternary faults and folds in Alaska: A digital database. Alaska Division of Geological & Geophysical Surveys, 141(July).

Langston, C. A. (1979). Structure under Mount Rainier, Washington, inferred from teleseismic body waves. *Journal of Geophysical Research*, *84*(B9), 4749–4762. https://doi.org/10.1029/JB084iB09p04749

Levshin, A. L., Ratnikova, L. I., & Berger, J. O. N. (1992). Peculiarities of surface wave propagation across central Eurasia. *Bulletin of the Seismological Society of America*, *82*(6), 2464–2493.

Martin-Short, R., Allen, R. M., & Bastow, I. D. (2016). Subduction geometry beneath south-central Alaska and its relationship to volcanism. *Geophysical Research Letters*, *43*, 9509–9517. https://doi.org/10.1002/2016GL070580

McNamara, D. E., & Pasayanos, M. E. (2002). Seismological evidence for a sub-volcanic arc mantle wedge beneath the Denali volcanic gap, Alaska. *Geophysical Research Letters*, *29*(16), 1814. https://doi.org/10.1029/2001GL014088

Miller, M. S., O'Driscoll, L. J., Porritt, R. W., & Roeske, S. M. (2018). Multiscale crustal architecture of Alaska inferred from P receiver functions. *Lithopshere*, *10*(2), 267–278.

Nelson, J., & Colpron, M. (2007). Tectonics and metallogeny of the British Columbia, Yukon and Alaskan Cordillera, 1.8 Ga to the present. *Mineral Deposits of Canada: A Synthesis of Major Deposit-Types, District Metallogeny, the Evolution of Geological Provinces, and Exploration Methods*, *2703*(5), 755–791.

Nockleberg, W. J., Parfenov, L. M., Monger, J. W. H., Norton, I. O., Khanchuk, A. I., Stone, D. B., et al. (2000). Phanerozoic tectonic evolution of the Circum-North Pacific. USGS Professional Paper, 1626 (pp. 1–122).

O'Driscoll, L. J., & Miller, M. S. (2015). Lithospheric discontinuity structure in Alaska, thickness variations determined by *Sp* receiver functions. *Tectonics*, *34*, 694–714. https://doi.org/10.1002/2014TC003669

Pavlis, T. L., Sisson, V. B., Foster, H. L., Nokleberg, W. J., & Plafker, G. (1993). Mid-Cretaceous extensional tectonics of the Yukon-Tanana Terrane, Trans-Alaska Crustal Transect (TACT), east-central Alaska. *Tectonics*, *12*(1), 103–122. https://doi.org/10.1029/92TC00860

Plafker, G., & Berg, H. (Eds.) (1994). The Geology of Alaska*Overview of the geology and tectonic evolution of Alaska*, *The Geology of North America series* (Vol. G-1, pp. 989–1021). America: Geological Society.

Porritt, R. W., & Miller, M. S. (2018). Updates to FuncLab, a Matlab based GUI for handling receiver functions. *Computers and Geosciences*, *111*, 260–271. https://doi.org/10.1016/j.cageo.2017.11.022

Porritt, R. W., Miller, M. S., & Darbyshire, F. A. (2015). Lithospheric architecture beneath Hudson Bay. *Geochemistry, Geophysics, Geosystems*, *18*, 1541–1576. https://doi.org/10.1002/2015GC005845

Pratt, M. J., Wysession, M. E., Aleqabi, G., Wiens, D. A., Nyblade, A. A., Shore, P., et al. (2017). Shear velocity structure of the crust and upper mantle of Madagascar derived from surface wave tomography. *Earth and Planetary Science Letters*, *458*, 405–417. https://doi.org/10.1016/j.epsl.2016.10.041

Preece, S. J., & Hart, W. K. (2004). Geochemical variations in the < 5Ma Wrangell Volcanic Field, Alaska: Implications for the magmatic and tectonic deveopment of a complex continental arc system. *Tectonophysics*, *392*(1-4), 165–191. https://doi.org/10.1016/j.tecto.2004.04.011

Randall, G. E. (1989). Efficient calculation of differential seismograms for lithospheric receiver functions. *Geophysical Journal International*, *99*(3), 469–481. https://doi.org/10.1111/j.1365-246X.1989.tb02033.x

Richter, D. H., Smith, J. G., Lanphere, M. A., Dalrymple, G. B., Reed, B. L., & Shew, N. (1990). Age progression of volcanism, Wrangell volcanic field, Alaska. *Bulletin of Volcanology*, *53*(1), 29–44. https://doi.org/10.1007/BF00680318

Rodi, W. L., Glover, P., Li, T. M. C., & Alexander, S. S. (1975). A fast, accurate method for computing group-velocity partial derivatives for Rayleigh and Love modes. *Bulletin of the Seismological Society of America*, *65*(5), 1105–1114.

Rondenay, S., Abers, G. A., & van Keken, P. E. (2008). Seismic imaging of subduction zone metamorphism. *Geology*, *36*(4), 275–278. https://doi.org/10.1130/G24112A.1

Rondenay, S., Montési, L. G. J., & Abers, G. a. (2010). New geophysical insight into the origin of the Denali volcanic gap. *Geophysical Journal International*, *182*(2), 613–630. https://doi.org/10.1111/j.1365-246X.2010.04659.x

Rossi, G., Abers, G. A., Rondenay, S., & Christensen, D. H. (2006). Unusual mantle Poisson's ratio, subduction, and crustal structure in Central Alaska. *Journal of Geophysical Research*, *111*, B09311. https://doi.org/10.1029/2005JB003956

Shellenbaum, D. P., Gregerson, L., & Delaney, P. (2010). Top Mesozoic unconformity depth map of the Cook Inlet Basin, Alaska. *Division of Geological & Geophysical Surveys Report of Investigation 2010–2*, 1 sheet (scale 1:500,000).

Shen, W., Ritzwoller, M. H., Schulte-Pelkum, V., & Lin, F. C. (2013). Joint inversion of surface wave dispersion and receiver functions: A Bayesianmonte-Carlo approach. *Geophysical Journal International*, *192*(2), 807–836. https://doi.org/10.1093/gji/ggs050

Stachnik, J. C., Abers, G. A., & Christensen, D. H. (2004). Seismic attenuation and mantle wedge temperatures in the Alaska subduction zone. *Journal of Geophysical Research*, *109*, B10304. https://doi.org/10.1029/2004JB003018

Trop, J. M., & Ridgway, K. D. (2007). Mesozoic and Cenozoic tectonic growth of southern Alaska: A sedimentary basin perspective. In K. D. Ridgway, J. M. Trop, J. M. G. Glen, & J. M. O'Neil (Eds.), *Tectonic growth of a collisional continental margin: Crustal evolution of south-central Alaska* (Vol. 2431, pp. 55–94). America: Geological Society.

Veenstra, E., Christensen, D. H., Abers, G. A., & Ferris, A. (2006). Crustal thickness variation in south-central Alaska. *Geology*, *34*(9), 781–784. https://doi.org/10.1130/G22615.1

Wang, Y., & Tape, C. (2014). Seismic velocity structure and anisotropy of the Alaska subduction zone based on surface wave tomography. *Journal of Geophysical Research: Solid Earth*, *119*, 8845–8865. https://doi.org/10.1002/2014JB011438

Ward, K. M. (2015). Ambient noise tomography across the southern Alaskan cordillera. *Geophysical Research Letters*, *42*, 3218–3227. https://doi.org/10.1002/2015GL063613

Ward, K. M., Zandt, G., Beck, S. L., Wagner, L. S., & Tavera, H. (2016). Lithospheric structure beneath the northern Central Andean Plateau from the joint inversion of ambient noise and earthquake-generated surface waves. *Journal of Geophysical Research: Solid Earth*, *121*, 8217–8238. https://doi.org/10.1002/2016JB013237

Wech, A. G. (2016). Extending Alaska's plate boundary: Tectonic tremor generated by Yakutat subduction. *Geology*, *44*(7), 587–590. https://doi.org/10.1130/G37817.1

Wessel, P., & Smith, W. H. F. (1998). New, improved version of generic mapping tools released. *Eos, Transactions American Geophysical Union*, *79*(47), 579–579. https://doi.org/10.1029/98EO00426

Witt, D. R. (2016). Seismic anisotropy in Northwestern Canada and Eastern Alaska from shear wave splitting measurements. Doctoral dissertation, Colorado State University Libraries.

Worthington, L. L., Van Avendonk, H. J. A., Gulick, S. P. S., Christeson, G. L., & Pavlis, T. L. (2012). Crustal structure of the Yakutat terrane and the evolution of subduction and collision in southern Alaska. *Journal of Geophysical Research*, *117*, B01102. https://doi.org/10.1029/2011JB008493